RESEARCH ARTICLE | JANUARY 06 2025

Impulse response of linear disturbances in a skewed Stokes layer

Christian Thomas ; Alexander Pretty

Physics of Fluids 37, 014107 (2025)
https://doi.org/10.1063/5.0249527

Physics of Fluids ARTICLE pubs.aip.org/aip/pof

Impulse response of linear disturbances in a skewed Stokes layer

Cite as: Phys. Fluids **37**, 014107 (2025); doi: 10.1063/5.0249527
Submitted: 18 November 2024 · Accepted: 12 December 2024 ·
Published Online: 6 January 2025

Christian Thomas[1,a] and Alexander Pretty[2]

AFFILIATIONS

[1]School of Mathematical and Physical Sciences, Macquarie University, NSW 2109, Australia
[2]School of Mathematics, Cardiff University, Cardiff CF24 4AG, United Kingdom

[a]Author to whom correspondence should be addressed: christian.thomas@mq.edu.au

ABSTRACT

The spatiotemporal development of impulsively excited two-dimensional linear disturbances in acceleration-skewed and velocity-skewed Stokes layers is investigated using numerical simulations of the linearized Navier–Stokes equations. This study focuses on the long-term behavior of linearly unstable disturbances within these skewed flows. The onset of linear instability in the symmetric Stokes layer is known to coincide with absolute instability, with disturbances forming family tree structures, characterized by multiple wavepackets spread across the spatiotemporal plane, coupled with pointwise subharmonic temporal growth [Ramage *et al.*, "Numerical simulation of the spatiotemporal development of linear disturbances in Stokes layers: Absolute instability and the effects of high-frequency harmonics," Phys. Rev. Fluids **5**, 103901 (2020)]. However, the introduction of acceleration and velocity skewness disrupts the formation of the family tree structure. Instead, the onset of linearly unstable behavior is matched to convective instability, with disturbances predominantly propagating in the direction of the maximum acceleration or maximum velocity. As the Reynolds number increases, absolute instability emerges, albeit with pointwise temporal growth less than the growth obtained by the disturbance maximum.

I. INTRODUCTION

Time-periodic flows are commonly observed in various physiological, environmental, and industrial processes. Examples include the pulsatile blood flow in arteries, the respiratory system in the lungs, and the propagation of waves in near-shore seas. Understanding the dynamics of these oscillating flows and their stability characteristics holds practical and theoretical significance for the field of fluid dynamics.

The Stokes layer represents a fundamental example of a time-periodic flow. It occurs when an infinite flat plate oscillates sinusoidally along the streamwise direction with a velocity $U_0\cos(\omega t)$, beneath a stationary semi-infinite layer of incompressible fluid. This oscillatory flow is characterized by a boundary layer thickness $\delta = \sqrt{2\nu/\omega}$, for the kinematic viscosity of the fluid, ν, and frequency of wall oscillation, ω. The Reynolds number of the flow is defined as $Re = U_0/\sqrt{2\nu\omega}$ and specifies regions of linear stability and instability as well as the transition to turbulence.

An early review of the Stokes layer and other related time-periodic flows was undertaken by Davis.[2] Since then, the Stokes layer has been the subject of numerous theoretical investigations relating to the linear stability of the flow, including quasi-steady instability theory,[3–5] Floquet theory,[6–9] and spatiotemporal disturbance development.[1,10,11] In addition, the effects of wall roughness have been considered[12–14] and several experimental studies modeled oscillatory motion in a channel and pipe.[15–18] More recently, investigations of oscillatory and pulsatile flows have focused on linear and nonlinear dynamics of the Floquet modal instability[19] and non-modal transient behavior.[20–22]

This paper is concerned with the spatiotemporal development of linear disturbances in a skewed Stokes layer, following the approach of Thomas *et al.*[10] and Ramage *et al.*,[1] for both acceleration-skewed[23] and velocity-skewed[24] oscillatory motion.

A. Floquet theory

The linear stability of both finite and semi-infinite geometries was initially investigated by Von Kerczek and Davis[6] and Hall,[7] respectively, using Floquet theory. This theory assumes that perturbations to the base flow can be expressed as the product of a time-periodic function, $f(\tau)$, and an exponential function, $\exp(\mu\tau)$, where τ denotes the non-dimensional time and the real part of the Floquet exponent, μ,

encapsulates the net growth of the linear disturbance. Due to the computational demands associated with the linear stability problem, these early investigations were limited to relatively low Reynolds numbers, Re. Hall[7] observed only decaying disturbances for Reynolds numbers $Re < 160$ in the semi-infinite Stokes layer, while Von Kerczek and Davis[6] found no linearly unstable modes for $Re < 400$ in the finite channel model they considered. Nevertheless, following significant improvements in computational resources, Blennerhassett and Bassom[8] identified linearly unstable behavior in the Stokes layer for a critical Reynolds number $Re_{s,c} \approx 708$. Their observations were later confirmed by Luo and Wu[5] and Thomas *et al.*[25] Moreover, similar methods were used to compute linear instability in related flows, including the finite Stokes layer in channels and pipes.[26–29]

B. Spatiotemporal disturbance development

While Floquet theory can identify the onset of linear instability, it cannot determine the nature of the instability, specifically whether it corresponds to convective or absolute instability. However, numerical simulations can be employed to analyze disturbance development by constructing wavepackets in the spatiotemporal plane. Convective instability arises when an unstable disturbance propagates away from the point of excitation (decaying at fixed spatial locations). On the other hand, a disturbance is absolutely unstable if it grows at every spatial location.[30]

The spatiotemporal development of two-dimensional linear disturbances in the semi-infinite Stokes layer was first considered by Thomas *et al.*[10] using numerical simulations of the linearized Navier–Stokes (LNS) equations. Using a velocity–vorticity form of the LNS equations,[31] Thomas and coworkers observed a so-called family tree structure within the spatiotemporal plane, characterized by the successive birthing of individual wavepackets. Although numerical computations were restricted to the first three periods of wall motion, excellent agreement was observed with the earlier Floquet analysis of Blennerhassett and Bassom.[8] Subsequent studies by Ramage[1,11] successfully simulated linear disturbance development for a longer duration for both the classical Stokes layer and the flow generated when the wall motion incorporates a form of low-amplitude, high-frequency noise.[32] The family tree structure was shown to be characterized by both harmonic and subharmonic phenomena. In addition, the longer-time simulations indicated that the onset of linear instability in the Stokes layer coincides with absolute instability instead of convective instability. Indeed, this was confirmed by Pretty *et al.*[9] using a modified form of the Briggs[33] method based on the formulation of Brevdo and Bridges.[34]

C. Skewed oscillatory flow

Wave propagation in near-shore seas is characterized by skewness, including wave depth, wave height, and wave period. Velocity skewness generates a wave with a narrow, sharp crest and a broad flat trough, whereas acceleration skewness establishes wave asymmetry [examples of each are depicted in Figs. 2(a) and 2(b)]. In coastal hydrodynamics, much of the focus is aimed at understanding how acceleration and velocity skewness affect the net transport of sediment.[35–41] For instance, experiments undertaken by Watanabe and Sato[40] and Abreu *et al.*[42] showed that in an acceleration-skewed oscillatory flow, the net sand transport is non-zero and propagates along the direction of maximum acceleration. In addition, acceleration skewness affects turbulent flows, including the emergence of streaky structures[43] and enhancing turbulent intensities in the flow over a rough surface.[44]

In the context of laminar flow, Thomas[23,24] undertook a linear stability analysis of the acceleration-skewed and velocity-skewed Stokes layers using Floquet theory. Modeling skewness via the methods developed by van der A *et al.*[44] and Scandura *et al.*[43] Thomas showed that acceleration skewness destabilizes the Stokes layer and reduces the critical Reynolds number for linear instability. On the other hand, velocity skewness increases the critical Reynolds number for linearly unstable behavior and stabilizes the flow.

D. The current investigation

In the following study, we consider the spatiotemporal development of two-dimensional linear disturbances in acceleration-skewed and velocity-skewed Stokes layers, using the numerical approach developed by Ramage *et al.*[1] The aim is to determine the nature of linearly unstable disturbances in these skewed flows, i.e., are disturbances matched to convective or absolute instability. Our investigation reveals that acceleration and velocity skewness alter the development of the family tree structure, with disturbances primarily propagating in one streamwise direction only, either to the right or the left, depending on the skewness specifications. Moreover, the onset of linear instability coincides with a convective form of instability rather than the absolute instability observed for the symmetric Stokes layer.[1,9,10] The latter form of instability is subsequently found to emerge at higher Reynolds numbers.

The remainder of this paper is structured as follows: in Sec. II, acceleration-skewed and velocity-skewed oscillatory wall motion are modeled, and the equations governing the development of linear disturbances are described. In Secs. III and IV, the results and conclusions of our study are presented.

II. FORMULATION

A. Base flow

Consider the two-dimensional flow that develops in a semi-infinite layer of viscous incompressible fluid that is bounded by a flat plate located in the plane $y^* = 0$. The wall oscillates back and forth along the streamwise x^*-direction with a skewed velocity $U_0 = U_0(t)$.[23,24,43,44] For an acceleration-skewed flow, the wall velocity is defined as

$$U_0(t) = U_{0,\max} \sum_{n=1}^{N} \gamma_n \sin(n(\omega t + \phi)), \tag{1a}$$

for a phase shift, ϕ, and coefficients

$$\gamma_n = \frac{\alpha(2\beta - 1)^{n-1}}{n}, \tag{1b}$$

that establishes asymmetric sinusoidal motion. On the other hand, for a velocity-skewed flow, the wall velocity is given as

$$U_0(t) = U_{0,\max} \sum_{n=1}^{N} \delta_n \cos(n(\omega t + \phi)), \tag{2a}$$

for $\delta_1 = 1$ and

$$\delta_n = \alpha(2\kappa - 1)^{n-1} \quad \text{for} \quad n \geq 2, \tag{2b}$$

that establishes oscillatory motion with a narrow sharp crest and a broad flat trough. Here, $U_{0,\max}$ is the maximum wall velocity, N is the total number of harmonics used to represent the wall motion, ω is the frequency of oscillation, and the coefficient, α, ensures $\max(U_0) = U_{0,\max}$. Figure 1 displays the relative sizes of α for both acceleration-skewed and velocity-skewed flows.

Acceleration skewness is quantified by the parameter

$$\beta = \frac{\dot{U}_{0,\max}}{\dot{U}_{0,\max} - \dot{U}_{0,\min}} \in [0, 1], \tag{3}$$

where $\dot{U}_0$ represents the acceleration of the wall motion. (Here, a dot denotes differentiation with respect to time, τ.) Whereas velocity skewness is quantified by the parameter

$$\kappa = \frac{U_{0,\max}}{U_{0,\max} - U_{0,\min}} \in [0, 1]. \tag{4}$$

The classical Stokes layer is recovered in each instance by setting $\beta = 0.5$ or $\kappa = 0.5$ for $N = 1$ harmonics. In the instance $\beta \neq 0.5$ or $\kappa \neq 0.5$, the number of harmonics, N, must be sufficiently large to achieve the desired skewed wall motion. Moreover, those flows generated for $\beta \in [0, 0.5]$ are the mirror images of those flows established for $\beta \in [0.5, 1]$. Similarly for $\kappa \in [0, 0.5]$ and $\kappa \in [0.5, 1]$. Consequently, the subsequent analysis is limited to those acceleration-skewed flows with $\beta \in [0.5, 1]$ and velocity-skewed flows with $\kappa \in [0.5, 1]$.

The dimensionless base flow is obtained by scaling the velocity and length on the respective scales $U_{0,\max}$ and $\sqrt{2\nu/\omega}$, where ν is the kinematic viscosity of the fluid. In addition, on setting $\tau = \omega t$, the non-dimensional base flow is given as

$$\boldsymbol{U}_B = (U_B(y, \tau; \beta, \kappa), 0), \tag{5a}$$

and for the acceleration-skewed flow

$$U_B(y, \tau; \beta) = \sum_{n=1}^{N} \gamma_n e^{-\sqrt{n}y} \sin\left(n(\tau + \phi) - \sqrt{n}y\right), \tag{5b}$$

while for the velocity-skewed flow

$$U_B(y, \tau; \kappa) = \sum_{n=1}^{N} \delta_n e^{-\sqrt{n}y} \cos\left(n(\tau + \phi) - \sqrt{n}y\right). \tag{5c}$$

Moreover, the Reynolds number of both acceleration-skewed and velocity-skewed flows is defined as

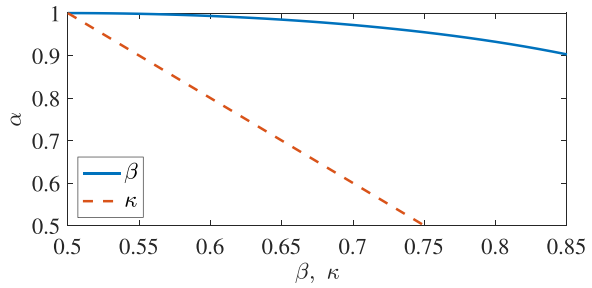

FIG. 1. Relative sizes of the coefficient α, as a function of the acceleration skewness, β, and velocity skewness, κ, that ensure $\max(U_0) = U_{0,\max}$.

$$Re = \frac{U_{0,\max}}{\sqrt{2\nu\omega}}. \tag{6}$$

Figure 2 illustrates the base flow, U_B, acceleration, $\dot{U}_B$, and shear stress, U_B', at the wall $y = 0$, for acceleration-skewed flows $\beta = 0.6$ and $\beta = 0.75$, and velocity-skewed flows $\kappa = 0.6$ and $\kappa = 0.75$. (Here, a prime denotes differentiation with respect to the wall-normal y-direction.) The wall motion of the classical Stokes layer (i.e., $\beta = \kappa = 0.5$) is included for comparison (solid blue lines).

B. Governing equations for linear disturbances

1. Velocity–vorticity formulation

The development of linear disturbances to the skewed base flow (5) is investigated using a two-dimensional version of the velocity–vorticity formulation developed by Davies and Carpenter.[31] This study focuses on the long-term behavior of linearly unstable disturbances, and since Squire's theorem has been extended to temporally periodic flows,[6] we limit our analysis to two-dimensional disturbances. Total velocity and vorticity fields are defined as

$$(U, V) = (U_B, 0) + (u, v), \tag{7a}$$

and

$$\Omega = \Omega_B + \zeta, \tag{7b}$$

where $\Omega_B = U_B'$ is the vorticity field associated with the base flow (5). Here, u and v denote the respective streamwise and wall-normal velocity perturbations, and ζ represents the vorticity perturbation.

Following the approach of Ramage,[1,11] a spectral treatment is implemented along the streamwise x-direction by decomposing linear disturbances into the following Fourier form:

$$\{u, v, \zeta\}(x, y, \tau) = \{u_j, v_j, \zeta_j\}(y, \tau) e^{ia_j x} + \text{c.c.}, \tag{8}$$

where c.c. denotes the complex conjugate and $a_j = j\Delta a$ specifies a discrete set of streamwise wavenumbers for $j = 0, \ldots, J$, and the wavenumber increment, Δa. The governing system of equations for each a_j comprises a vorticity transport equation for ζ_j and the Poisson equation for v_j

$$\frac{1}{Re}\frac{\partial \zeta_j}{\partial \tau} + ia_j U_B \zeta_j + U_B'' v_j = \frac{1}{2Re}\left(\frac{\partial^2}{\partial y^2} - a_j^2\right)\zeta_j, \tag{9a}$$

$$\left(\frac{\partial^2}{\partial y^2} - a_j^2\right) v_j = -ia_j \zeta_j. \tag{9b}$$

In addition, the streamwise u_j-velocity perturbation is given by the integral expression

$$u_j = -\int_y^\infty (\zeta_j + ia_j v_j)\, dy. \tag{10}$$

Perturbations are impulsively excited by a small temporally and spatially localized vertical wall displacement, η. The linearized boundary conditions are then implemented through the no-slip and no-penetration conditions

$$u_j(0, \tau) = -U_B'(0, \tau)\eta_j(\tau), \tag{11a}$$

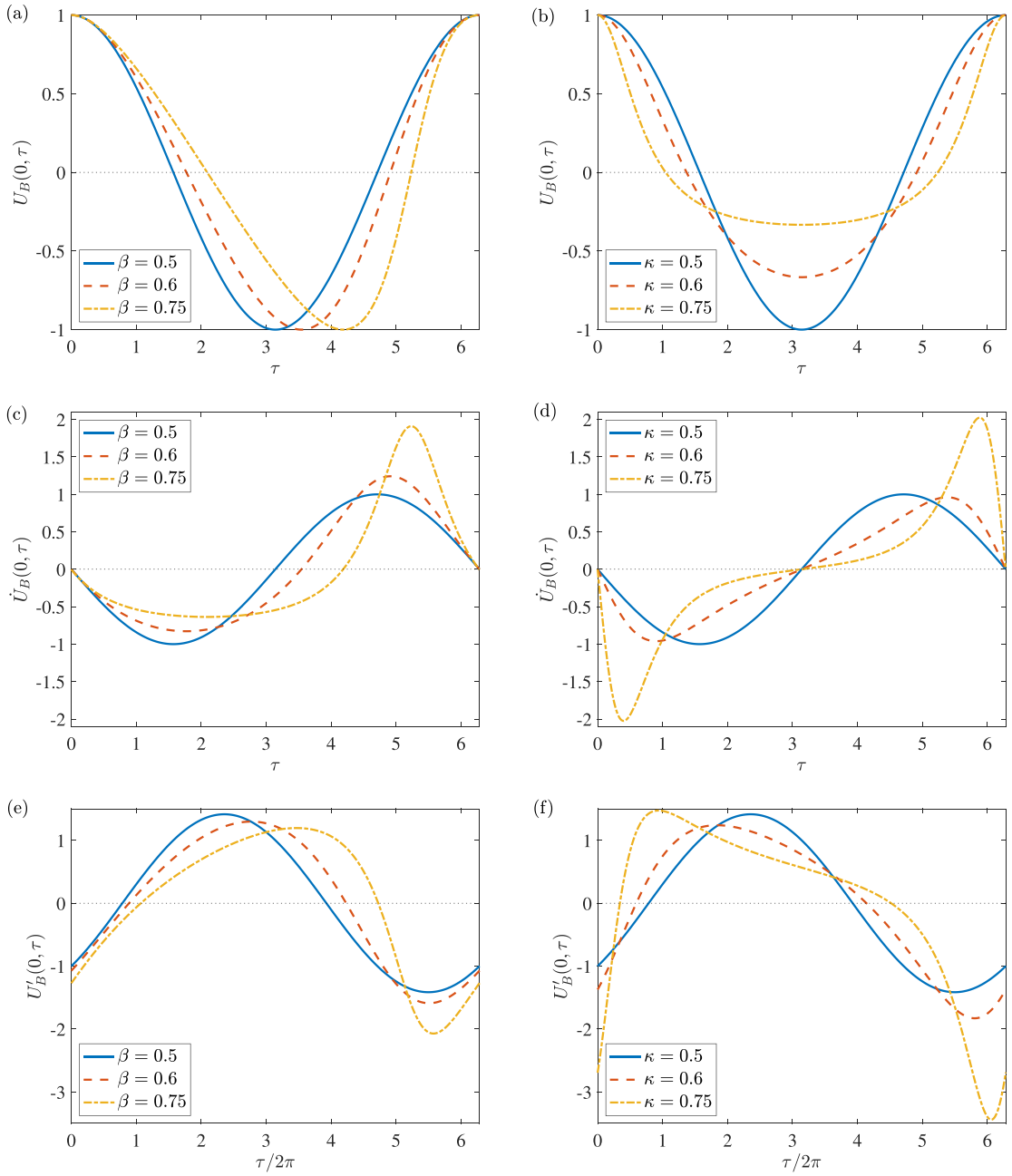

FIG. 2. Base flow, U_B, acceleration, $\dot{U}_B$, and shear stress, U_B', at the wall, as a function of time, τ. (a), (c), and (e) Acceleration-skewed flow for variable β. (b), (d), and (f) Velocity-skewed flow for variable κ. The phase shift, ϕ, is chosen to ensure $U_B(0,0) = 1$.

$$v_j(0,\tau) = \frac{\partial \eta_j}{\partial \tau}, \tag{11b}$$

where η_j represents a Fourier j-component of the decomposed vertical wall displacement, η. The localized impulsive forcing is defined by setting

$$\eta(x,\tau) = \mathrm{e}^{-b(x-x_f)^2}(1-\mathrm{e}^{-\sigma\tau^2})\mathrm{e}^{-\sigma\tau^2} \simeq \frac{1}{J+1}\sum_{j=0}^{J}\eta_j(\tau)\mathrm{e}^{\mathrm{i}(j\Delta a)x}, \tag{12}$$

where σ prescribes the time duration of the impulse, b is a scale factor that determines the spread of the forcing along the streamwise x-direction, and x_f (set to zero here) denotes the location about which the

impulse is centered. The parameter σ is chosen to ensure that for $\tau > 0.1$, the wall displacement, η, is essentially zero, while the scale factor, b, is chosen such that Fourier coefficients, η_j, have equal weighting. Finally, an integral constraint on the vorticity perturbation, ζ_j, is derived by coupling the definition for the streamwise u_j-velocity in Eq. (10) with the no-slip condition (11a) to give

$$\int_0^\infty \zeta_j \, \mathrm{d}y = U_B'(0,\tau)\eta_j(\tau) - \int_0^\infty \mathrm{i}a_j v_j \, \mathrm{d}y. \tag{13}$$

The temporal evolution of each Fourier j-component of the total linear disturbance (8) is computed independently; a decoupling arises due to the spatial homogeneity of the base flow and the linearity of the governing equations. The full spatiotemporal disturbance development established by the localized impulsive wall forcing, η, can be reconstructed by superimposing all Fourier j-components. Key to this reconstruction is the size of the wavenumber increment, Δa, which naturally establishes a spatial periodicity of $2\pi/\Delta a$. To ensure the spatial development of disturbances is captured in full detail, Δa is chosen to be sufficiently small. In addition, the range of streamwise wavenumbers $a_j \in [0, a_{\max}]$ for $a_{\max} = J\Delta a$, has to be large enough to ensure that both large and small stability characteristics are resolved accurately.

In the subsequent study, $\Delta a = 2.5 \times 10^{-4}$ ensured that the periodic box was sufficiently large that the disturbance remained far from the periodic boundaries for the ten periods of wall motion simulated. A choice of $a_{\max} = 0.6$ was sufficient to achieve accurate results since Fourier j-components at larger wavenumbers were subject to rapid temporal decay.

2. Numerical methods

The governing system of Eq. (9) is solved using the numerical scheme developed by Davies and Carpenter[31] that implements a spectral discretization along the wall-normal y-direction. The wall-normal velocity and vorticity perturbations, $q_j = \{v_j, \zeta_j\}$, are expanded in terms of an odd Chebyshev series

$$q_j(y,\tau) = \sum_{k=1}^{M} q_{j,k}(\tau) T_{2k-1}(\xi), \tag{14}$$

where T_k is the kth Chebyshev polynomial of the first kind, M is the number of Chebyshev polynomials, and ξ denotes the mapped wall-normal coordinate. Here, the semi-infinite physical domain $y \in [0, \infty)$ is mapped onto $\xi \in (0, 1]$ via the transformation

$$\xi = \frac{L}{L+y}, \tag{15}$$

where L is a stretching parameter that fixes the spread of data points along the Stokes layer. A similar expansion is implemented for the streamwise u_j-velocity in terms of even Chebyshev polynomials in ξ. Equations (9) are integrated twice with respect to the mapped wall-normal coordinate, ξ, and the evolution of the linear perturbation is numerically simulated using a semi-implicit procedure.

3. Reconstructing the physical disturbance development

The full spatiotemporal disturbance development can be reconstructed by taking a superposition of all Fourier j-components of the linear disturbance (8), for each streamwise wavenumber, $a_j \in [0, 0.6]$. (Recall $a_j = j\Delta a$ for $j = 0, \ldots, J$, and $\Delta a = 2.5 \times 10^{-4}$.) For instance, the vorticity perturbation, ζ, at each streamwise x-position, can be determined by setting

$$\zeta(x,y,\tau) = \sum_{j=0}^{J} \zeta_j(y,\tau) \mathrm{e}^{\mathrm{i}a_j x}. \tag{16}$$

The streamwise domain was chosen to be sufficiently large to satisfy the previously described natural spatial periodicity of $2\pi/\Delta a$. In addition, perturbation fields were computed at the streamwise locations $x = x_j = j\Delta x$, for $\Delta x = 2\pi/((J+1)\Delta a)$.

In addition to selecting a sufficiently small wavenumber increment, Δa, to capture the linear disturbance development in full, the number of Chebyshevs, M, and the mapping parameter, L, were chosen based on previous experience with this numerical approach.[1,11,25] In this study, setting $M = 96$ and $L = 4$ produced accurate solutions, as further increases in M or varying L did not alter the results. Moreover, the time step in the time-marching procedure was defined as $\Delta\tau = 0.1/Re$, which allowed $O(10^4)$ time steps per period of oscillation.

III. RESULTS

A. Stokes layer

To better understand the observations of Thomas *et al.*[10] and Ramage *et al.*[1] on the development of linear disturbances in the Stokes layer, and the relation to the current investigation, we first reproduce the stability characteristics of the family tree structure. The Stokes layer is established by setting $\kappa = 0.5$ in Eq. (5c) for the velocity-skewed flow. Alternatively, setting $\beta = 0.5$ in Eq. (5b) establishes the Stokes layer but with a phase shift of $\pi/2$. (Recall the formula for the acceleration-skewed and velocity-skewed flows in Sec. II A.) Figure 3 illustrates the spatiotemporal development of two linear disturbances, impulsively excited at $x_f = 0$, with Reynolds number $Re = 715$, which corresponds to linearly unstable conditions.[8] (Recall the critical Reynolds number for linear instability is $Re_{s,c} \approx 708$.) Contours are based on the logarithm of the absolute valued wall vorticity perturbation, $\ln|\zeta|$, and solutions are plotted in the non-dimensional $(x, \tau/2\pi)$-plane, where $\tau/2\pi$ denotes the number of wall oscillations. In addition, each solution is normalized on the maximum absolute value attained during the first period of wall motion, $\tau \in [0, 2\pi]$.

In Fig. 3(a), the impulse is imposed at time $\tau = 0$ for a phase shift $\phi = 0$, while in Fig. 3(b), a phase shift of half a period is implemented with $\phi = \pi$. The phase shift, ϕ, is chosen to ensure the wall velocity at time $\tau = 0$ is $U_B(0,0) = 1$ in Fig. 3(a) and $U_B(0,0) = -1$ in Fig. 3(b). Initially, the acceleration of the oscillating wall is zero in both cases but then passes into the deceleration phase for the former case and the acceleration phase for the latter case. Due to the symmetry of the Stokes layer, the half-period phase-shift between these cases results in an exact reversal of the direction of the flow at any point in space and time. The disturbance development presented in Fig. 3(b) is therefore the mirror image of that shown in Fig. 3(a), reflected about a vertical line at $x = 0$.

Focusing on the behavior illustrated in Fig. 3(a), the initial impulse excites a disturbance wavepacket that propagates to the right. [The behavior is reversed in Fig. 3(b).] Subsequently, this initial parent wavepacket births two child wavepackets during each period of wall oscillation: one convects to the left and one to the right of the parent

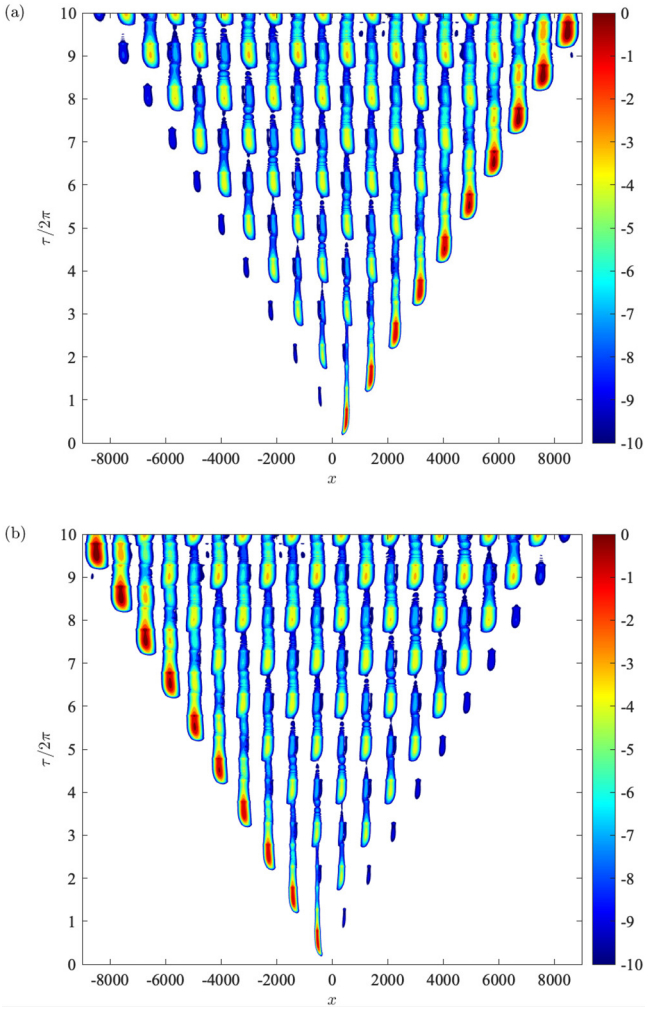

FIG. 3. Spatiotemporal contour plots of the linear disturbance in the Stokes layer with Reynolds number $Re = 715$. Contours are based on the logarithm of the absolute valued wall vorticity perturbation, $\ln|\zeta|$. Disturbances are impulsively excited at $x_f = 0$ for the base flow given in Eq. (5c) with $\kappa = 0.5$ and a phase shift (a) $\phi = 0$ and (b) $\phi = \pi$. Solutions are normalized on $\max_{x,\tau\in[0,2\pi]}|\zeta|$.

wavepacket. The birthing of each child wavepacket coincides with the wall shear stress, U_B', changing sign. A negative to positive change in the wall shear stress excites the wavepacket that convects to the right. On the other hand, the left convecting wavepacket is brought about by a positive to negative reversal in the wall shear stress. Each child wavepacket births two further grandchild wavepackets, and so on, leading to the formation of the family tree structure.

The disturbance maximum convects along those wavepackets found on the right-hand side of the family tree formation [and the left-hand side in Fig. 3(b)], with the temporal development of the maximum wall vorticity, $\max_x|\zeta|$, plotted in Fig. 4(a). There is a small increase in the disturbance amplitude from one period of wall oscillation to the next, which is a clear indication of linear instability.

Assuming that disturbances display behavior consistent with Floquet stability theory, we can derive expressions for computing temporal growth rates. Disturbances have the form $F(\tau) = \exp(\mu\tau)f(\tau)$, where F represents a disturbance field such as the wall vorticity, ζ, f is 2π-periodic in τ, and the real part of the complex Floquet exponent, μ, denotes the temporal growth rate. The temporal growth rate associated with the disturbance maximum was computed using the formula

$$\mu_m(\tau) = \frac{1}{2\pi}\ln\left(\frac{\max_x|\zeta(x, y = 0, \tau + 2\pi)|}{\max_x|\zeta(x, y = 0, \tau)|}\right). \tag{17}$$

Here, $\max_x|\zeta(x, 0, \tau)|$ was measured about the mid-point of each cycle of wall motion. The corresponding growth rate, μ_m, plotted in Fig. 4(d) (solid blue line), approaches a positive value for large time, τ, indicating linear instability. Indeed, as time increases, μ_m approaches the value of the real part of the Floquet exponent, μ, obtained via the Floquet theory.[8] For larger Reynolds numbers, Re, larger temporal growth rates and stronger linearly unstable behavior ensue.

The streamwise location, $x_{\max}$, of the disturbance maximum is plotted as a function of time in Fig. 4(b). Here, blue star markers indicate the corresponding x-location as measured at the mid-point of each wall cycle and the solid line represents the line of best fit. There is a distinct, fixed spacing between successive disturbance wavepackets, with the maximum amplitude propagating a streamwise distance $\Lambda \approx 850$ units from one period of wall oscillation to the next. Moreover, it was shown by Ramage *et al.*[1] that the streamwise spacing, Λ, between all neighboring parent and child wavepackets is proportional to the Reynolds number, Re.

In addition to the Λ-spacing between adjacent wavepackets, the distance 2Λ corresponds to the spacing between disturbance wavepackets of commensurate size. For instance, at time $\tau/2\pi = 4$ in Fig. 3(a), there are three distinct wavepackets with amplitudes of the order $\ln|\zeta| \approx -5$ (green-turquoise contours) located about the streamwise positions $x \approx -2000$, $x \approx -300$, and $x \approx 1400$, separated by a streamwise distance of 2Λ. Similarly, at the same point in time, a second set of smaller-sized wavepackets, of the order $\ln|\zeta| \approx -7$, develop about the mid-point between the first set of larger-sized wavepackets, i.e., at $x \approx -1200$, $x \approx 500$, and $x \approx 2200$. Analogous behavior is observed at other points in time. Thus, aside from the wavepacket containing the disturbance maximum that is convected along the outermost right wavepackets, the family tree structure is symmetric about $x = 0$ and characterized by a 2Λ-spatial periodicity.

Finally, at fixed streamwise x-locations, the disturbance exhibits subharmonic temporal growth. This particular observation is best demonstrated in Fig. 4(c), with the temporal development of the absolute valued wall vorticity, $|\zeta|$, plotted at the two fixed streamwise x-positions, $x = 500$ and $x = 1400$. On ignoring the first two cycles of wall motion (due to transient behavior), a peak amplitude is realized about odd-valued $\tau/2\pi$ at $x = 500$, whereas a maximum amplitude is attained for even-valued $\tau/2\pi$ at $x = 1400$. Moreover, at both streamwise x-locations, the amplitude increases in size every two periods. Hence, subharmonic behavior with periodicity twice that of the basic state emerges. Remarkably, the pointwise growth rate, μ_0, at these fixed x-positions is comparable with the growth rate of the disturbance maximum, μ_m. Indeed, computing the pointwise growth rate using

$$\mu_0(\tau) = \frac{1}{4\pi}\ln\left(\frac{|\zeta(x, y = 0, \tau + 4\pi)|}{|\zeta(x, y = 0, \tau)|}\right), \tag{18}$$

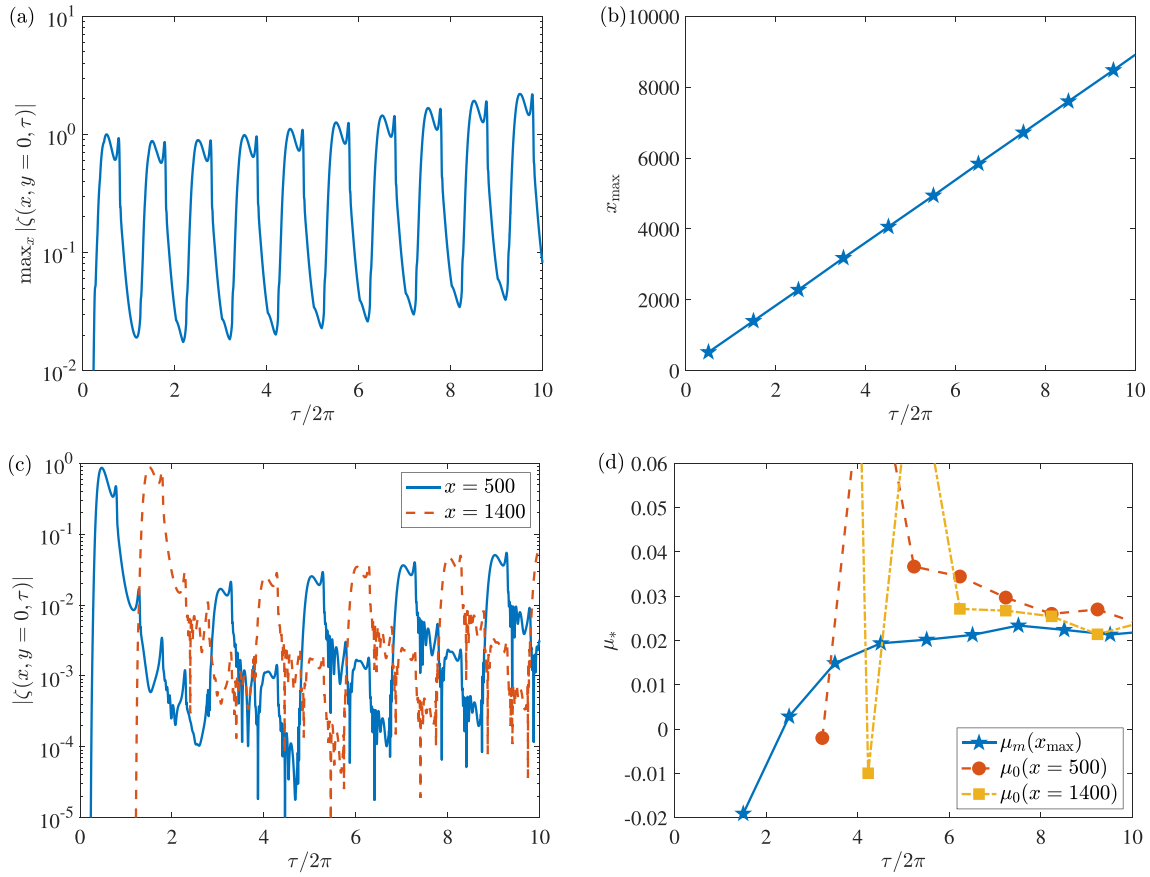

FIG. 4. Disturbance characteristics of the family tree structure presented in Fig. 3(a). (a) Temporal development of the maximum amplitude of the wall vorticity perturbation, $\max_x|\zeta|$. (b) Streamwise location, x_{max}, at which the maximum occurs at the mid-point of each wall cycle (blue star markers) and line of best fit (solid blue line). (c) Temporal development of the absolute valued wall vorticity perturbation, $|\zeta|$, at two fixed streamwise x-locations: $x = 500$ (solid blue) and $x = 1400$ (dashed red). (d) Temporal growth rate, μ_m, of the disturbance maximum in (a) (solid blue) and pointwise growth rate, μ_0, at the fixed x-locations in (c).

at $x = 500$ and $x = 1400$, establishes the dashed red line (for $x = 500$) and chain yellow line (for $x = 1400$) shown in Fig. 4(d). As time increases, the pointwise growth rate, μ_0, at each location approaches a similar (positive) value to the growth of the disturbance maximum, μ_m. Thus, the disturbance displays absolutely unstable behavior, as confirmed separately by Pretty, Davies, and Thomas[9] using a modified Briggs[33] and Brevdo and Bridges[34] approach.

B. Acceleration-skewed Stokes layer

1. Disturbance development in the flow β=0.6

Linear disturbance development in an acceleration-skewed Stokes layer is established for the acceleration skewness parameter $\beta = 0.6$. (Setting $\beta = 0.4$ generates the same resulting behavior as that presented here but with the direction of disturbance development flipped due to a reversal of the acceleration and deceleration phases of the oscillatory wall motion.) In addition, the number of harmonics, N, in the definition of the acceleration-skewed base flow (5b), was chosen to be sufficiently large to ensure the asymmetric wall motion was smooth and disturbance development unchanged by further increases in N. Following the Floquet stability analysis undertaken by Thomas,[23,24] $N = 20$ harmonics were used here and for all subsequent skewness configurations modeled.

The impulse response of two linear disturbances, excited about $x_f = 0$, is depicted in Fig. 5 for the unstable Reynolds number $Re = 635$; Floquet theory[23] predicts the critical Reynolds number $Re_c \approx 630$ for $\beta = 0.6$. In Fig. 5(a), the phase shift, ϕ, is chosen to ensure the base flow at the wall at time $\tau = 0$ is $U_B(0, 0) = 1$, and in Fig. 5(b), ϕ is set so $U_B(0, 0) = -1$, i.e., the wall acceleration is initially zero in both cases, but with the flow transitioning into the decelerating phase in the former case and the accelerating phase in the latter case (recall Fig. 2). Like those contour plots presented in Fig. 3, disturbance development is again based on the logarithm of the absolute valued wall vorticity, $\ln|\zeta|$, and normalized on the maximum absolute value attained during the first period of wall motion.

The initial response to the impulsive forcing is similar to that presented in Fig. 3 for the Stokes layer. A parent wavepacket is established that propagates to the right in Fig. 5(a) and the left in Fig. 5(b). Similarly, two child wavepackets are birthed by the parent that propagate a spatial distance, Λ, to the left and right, with the birthing event

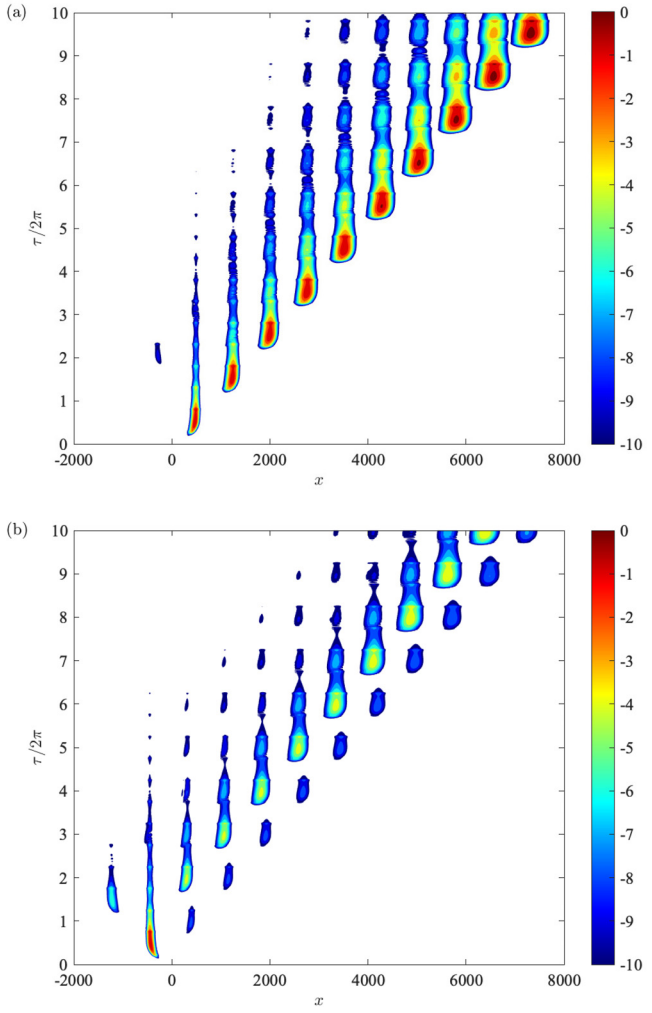

FIG. 5. Spatiotemporal contour plots of the linear disturbance in an acceleration-skewed Stokes layer with $\beta = 0.6$ and Reynolds number $Re = 635$. Contours are based on the logarithm of the absolute valued wall vorticity perturbation, $\ln|\zeta|$. Disturbances are impulsively excited at $x_f = 0$ for a phase shift (a) $\phi = 1.37$ and (b) $\phi = 4.91$. Solutions normalized on $\max_{x,\tau\in[0,2\pi]}|\zeta|$ and the phase shift, ϕ, is chosen to ensure $U_B(0,0) = 1$ in (a) and $U_B(0,0) = -1$ in (b).

again coinciding with a reversal of the wall shear stress, U_B'. However, beyond these initial, comparable wavepacket formations, disturbance development is distinctly different from that found for the Stokes layer. Left propagating wavepackets dissipate and, except for two small-sized wavepackets (one in each subplot), develop at magnitudes below the low-amplitude cutoff, i.e., $\ln|\zeta| < -10$. In addition, despite the two disturbances being excited at different phases of the acceleration-skewed wall motion, only the right propagating wavepackets remain, with the disturbance maximum passing through the right-most wavepackets in Fig. 5(a) (dark red contours) and the second to right-most wavepackets in Fig. 5(b) (yellow contours). Thus, disturbance development is predominantly directed to the right. Indeed, this particular disturbance feature was observed for other phase shifts $\phi \in [0, 2\pi)$. In the case depicted in Fig. 5(b), the smaller magnitude of the disturbance maximum and the fact that this occurs in the second rightmost wavepacket is a consequence of the disturbance initially propagating to the left in the spatiotemporal plane.

Acceleration skewness, for $\beta > 0.5$, increases the amplitude of acceleration, $\dot{U}_B$, during the accelerating phase of wall motion and reduces the amplitude of $\dot{U}_B$ during the decelerating phase. Furthermore, acceleration skewness establishes a longer period of positive shear stress, U_B', at the wall [see Fig. 2(e)]. Consequently, the disturbance is characterized by large-sized right propagating wavepackets only. The reverse is true for $\beta < 0.5$. In addition, while the Λ-spacing between neighboring wavepackets persists, the 2Λ-spatial periodicity has vanished since all wavepackets at a given time are of different sizes. Moreover, at fixed streamwise x-locations, the magnitude of the disturbance decreases, attaining values below the low-amplitude cutoff within 5–6 periods of wall motion. Thus, the disturbance does not exhibit pointwise temporal growth, nor the subharmonic phenomenon previously observed for the symmetrical Stokes layer. Therefore, the symmetry of the family tree structure is lost, and the onset of linear instability is characterized by convective behavior rather than the absolute form of instability found for the Stokes layer.

Figure 6 displays the temporal development of the disturbance maximum, $\max_x|\zeta|$, and the corresponding streamwise location, $x_{\max}$, of the two disturbances plotted in Fig. 5. Similar to Fig. 4(b), the streamwise location, $x_{\max}$, in Fig. 6(b) is plotted at the mid-point of each wall cycle, along with the line of best fit. With the notable exception of the respective size differences in $\max_x|\zeta|$ and $x_{\max}$, due to the phase at which each disturbance is initially excited, the long-term trends are similar. Each disturbance maximum, $\max_x|\zeta|$, exhibits a marginal increase in amplitude from one period to the next, and the corresponding location, $x_{\max}$, increases by $\Lambda \approx 750$ after each successive period of wall motion.

Figure 5 demonstrates that the asymmetry brought about by acceleration skewness results in the breakdown of the family tree structure. Notably, the onset of linear instability now aligns with convective instability rather than absolute instability. To further illustrate this behavior, additional stability characteristics are presented in Fig. 7. Figure 7(a) displays instantaneous snapshots of the absolute valued wall vorticity, $|\zeta|$, at four successive points in time. The plot demonstrates the propagation of the disturbance to the right with increasing time, τ. In addition, results illustrate the pointwise decay observed at fixed streamwise x-locations. For instance, a considerable reduction in $|\zeta|$ is observed at $x \approx 1250$. Similarly, at $x \approx 2000$ and $x \approx 2750$.

The wavenumber power spectra, P, of the wall vorticity, ζ, are plotted in Fig. 7(b). Here, P is computed by taking a Fast Fourier Transform of the reconstructed, physical vorticity perturbation at the wall, $\zeta(x, 0, \tau)$, at those four times shown in Fig. 7(a). The distributions of P are all centered about a narrowing range of wavenumbers, a, with the peaks located about $a \approx 0.385$, which is consistent with the Floquet stability calculations of Thomas.[23] This corresponds to a wavelength $\lambda = 2\pi/0.385 \sim 16$ and is comparable with that observed for the Stokes layer,[10] with each of the larger-sized wavepackets extending over a distance of approximately 20 wavelengths, λ.

In Fig. 7(c), the temporal development of the disturbance is plotted at three streamwise locations, which coincide with the center of the parent, child, and grandchild wavepackets to the immediate right of the impulsive forcing. The plot demonstrates pointwise temporal decay,

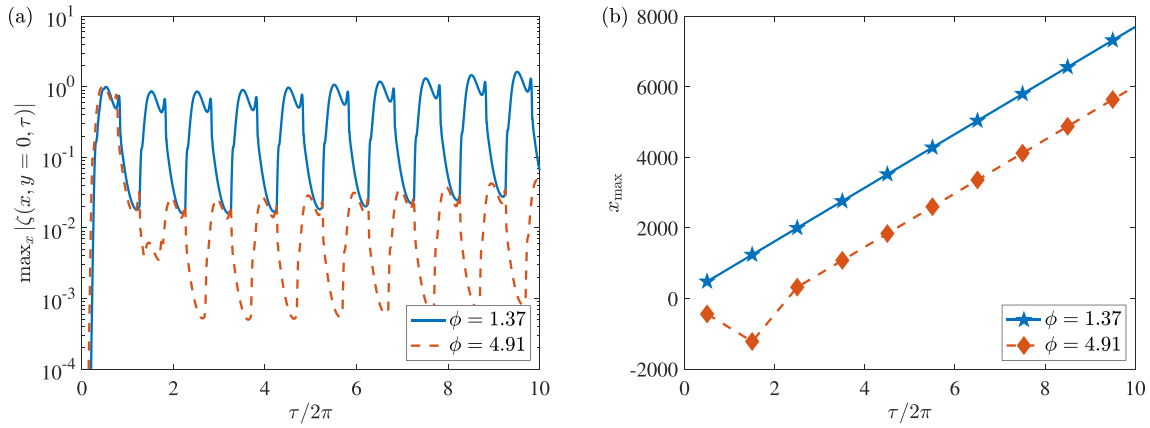

FIG. 6. Characteristics of the linear disturbance plotted in Fig. 5, with $\beta = 0.6$ and $Re = 635$. (a) Temporal development of the maximum amplitude of the wall vorticity perturbation, $\max_x|\zeta|$. (b) Streamwise location, $x_{\max}$, at which the maximum occurs at the mid-point of each wall cycle (star and diamond markers) and the lines of best fit (solid and dashed lines).

with the amplitude of the disturbance decreasing by several orders of magnitude over the time interval shown. Moreover, the pointwise temporal growth rate, μ_0, at these fixed streamwise locations, approaches a negative value of $\mu_0 \approx -0.1$ for large time, $\tau/2\pi$, compared with the positive-valued temporal growth rate, μ_m, obtained for the disturbance maximum [see Fig. 7(d)]. In addition, the subharmonic behavior observed for the Stokes layer is replaced with periodic decay at $x = 1250$ and $x = 2000$, and a half-periodic decay at $x = 500$.

Further disturbance development was simulated for $\beta = 0.6$ at higher, linearly unstable Reynolds numbers. The aim being to determine whether absolute instability emerges at larger Reynolds numbers or if the convective behavior persists. Figure 8 depicts the wavepacket formations for the Reynolds numbers $Re = 650$ and $Re = 675$, with the phase shift, ϕ, again set to 1.37 to ensure $U_B(0, 0) = 1$. In both instances, the disturbance exhibits convectively unstable behavior, as each parent wavepacket gives rise to larger-sized right-propagating wavepackets, indicating strong temporal growth. As before, left propagating wavepackets develop at magnitudes below the low-amplitude cutoff. Moreover, the disturbance is similarly diminished at fixed streamwise x-locations, with the size of the disturbance less than the low-amplitude cutoff within one or two periods of wall motion. Thus, disturbances are again characterized by pointwise temporal decay and convective instability, even at these relatively large Reynolds numbers.

2. Onset of linear instability

The temporal development of the disturbance maximum is illustrated in Fig. 9 for four Reynolds numbers, from $Re = 600$ through to $Re = 675$, with the acceleration skewness parameter again given as $\beta = 0.6$. A noticeable reduction in the disturbance amplitude emerges at $Re = 600$ and a notable growth at $Re = 650$ and $Re = 675$. The temporal growth rate, μ_m, associated with each disturbance maximum was computed via Eq. (17). The large time asymptotic values of μ_m (as measured at time $\tau/2\pi = 10$) for $\beta = 0.6$ are indicated by red circular markers in Fig. 10(a), with the red dashed line representing the line of best fit. In addition, similar results are shown for the Stokes layer $\beta = 0.5$ (blue solid line and star markers) and the stronger acceleration-skewed flow $\beta = 0.75$ (yellow chain line and square markers). In each case, the temporal growth rate exhibits an almost linear increase with the Reynolds number, Re, like that shown in Blennerhassett and Bassom[8] and Thomas *et al.*,[25] with the onset of linear instability (i.e., $\mu_m = 0$) consistent with the Floquet stability calculations.[23] Furthermore, Fig. 10(a) highlights the significant destabilizing effect due to acceleration skewness, with the critical Reynolds number, Re_c, decreasing as β increases.

Table I compares the critical Reynolds numbers, Re_c, as computed from Fig. 10(a), with the results of the Floquet theory.[23] The Re_c values are consistent across both methods, providing validation for the current numerical approach. The minor differences in Re_c can be attributed to the finite simulation time for disturbance development, and with longer numerical simulations, we would expect these differences to diminish.

Figure 10(b) displays the streamwise distance, Λ, between neighboring disturbance wavepackets in the spatiotemporal plane, as a function of the Reynolds number. Solutions are given for those acceleration skewness, β, and Reynolds numbers, Re, modeled in Fig. 10(a). In each instance, Λ increases linearly with Re, with nearly identical gradients. However, at fixed Reynolds numbers, the distance Λ between adjacent wavepackets decreases as β increases. Specifically, Λ is approximately 20 and 60 streamwise units greater in the case of the Stokes layer, $\beta = 0.5$, compared to the acceleration-skewed flows $\beta = 0.6$ and $\beta = 0.75$, respectively. Thus, as the acceleration skewness of the oscillatory flow increases, the distance between adjacent wavepackets decreases.

3. Disturbance development for flows $\beta \in [0.5, 0.54]$

The above results indicate that the onset of linear instability in acceleration-skewed Stokes layers corresponds to convective instability. However, it is unclear whether this behavior persists for all Reynolds numbers, Re, or if absolute instability eventually sets in. In the case $\beta = 0.6$, the analysis was limited to Reynolds numbers $Re \leq 675$ due to the considerable temporal growth rate, μ_m, observed at large Re. Indeed, in Fig. 8(b), wavepackets attained amplitudes large enough to induce significant round-off errors that limited the analysis to the first six periods of wall motion. Thus, extending disturbance development

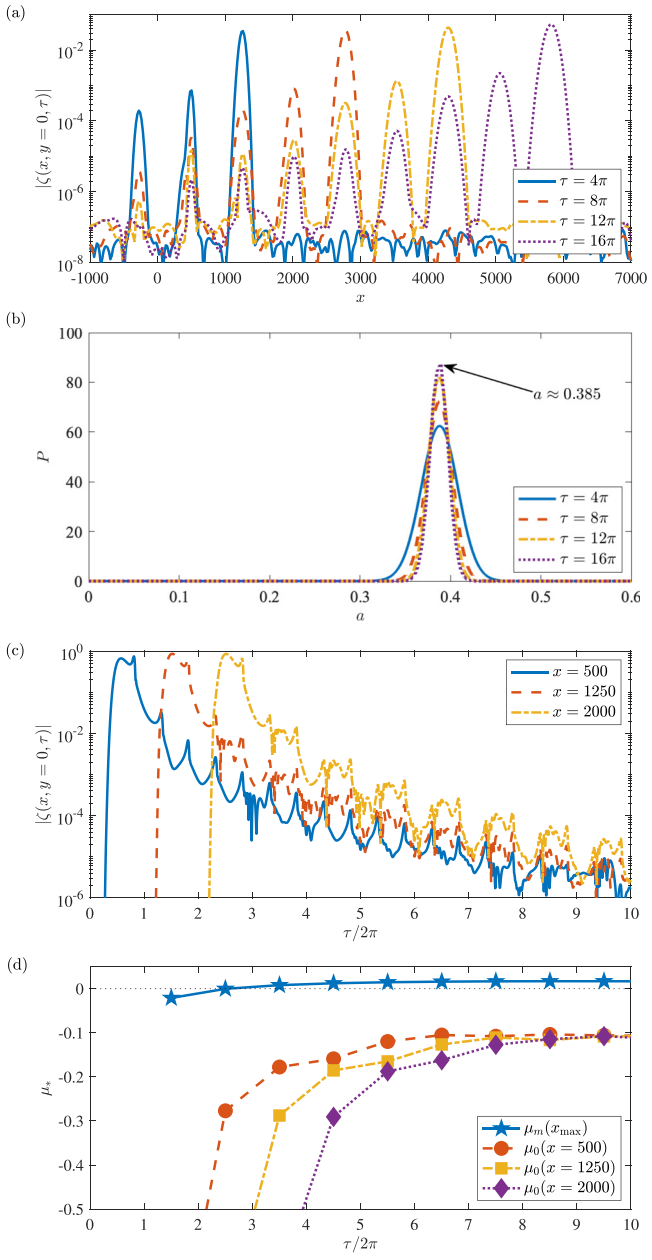

FIG. 7. Characteristics of the linear disturbance plotted in Fig. 5(a), with $\beta = 0.6$, $Re = 635$, and $\phi = 1.37$. (a) Instantaneous snapshots of the absolute valued wall vorticity perturbation, $|\zeta|$, at time $\tau = 4\pi$ (solid blue line), $\tau = 8\pi$ (dashed red), $\tau = 12\pi$ (chain yellow), and $\tau = 16\pi$ (dotted purple). (b) Wavenumber power spectra, P, plotted at those times given in (a). (c) Temporal development of $|\zeta|$ at three fixed streamwise x-locations: $x = 500$ (solid blue line), $x = 1250$ (dashed red), and $x = 2000$ (chain yellow). (d) Temporal growth rate, μ_m, along the disturbance maximum (solid blue line), and pointwise growth rate, μ_0, at the three fixed x-locations given in (c).

beyond that illustrated above proved very difficult. Moreover, it was impossible to establish distinct wavepacket structures in the spatiotemporal plane at $Re > 675$ or accurately trace the pointwise evolution of the disturbance.

In an attempt to predict the behavior of disturbances at large Reynolds numbers, Re, and ascertain whether the loss of the family tree structure occurs immediately following the introduction of acceleration skewness, further disturbances were simulated for acceleration-skewed flows $\beta \in [0.5, 0.54]$. Figure 11 depicts spatiotemporal contour plots for $\beta = 0.5$ (i.e., the Stokes layer), $\beta = 0.52$, and $\beta = 0.54$. Solutions on the left correspond to $Re = 700$, and the right to $Re = 715$. Contour plots reaffirm several stability features brought about by acceleration skewness. First, acceleration skewness induces a significant destabilizing effect, with disturbances for $\beta = 0.54$ [see Figs. 11(e) and 11(f)] attaining considerably larger amplitudes than those realized for $\beta = 0.5$ [see Figs. 11(a) and 11(b)]. Second, the symmetry of the family tree structure, including the 2Λ-spatial periodicity between similar-sized wavepackets, disappears following the application of acceleration skewness, with disturbance development predominantly directed to the right and along the positive x-direction. This is especially true for those cases plotted on the left of Fig. 11. For $Re = 700$ and $\beta = 0.52$ and $\beta = 0.54$ [see Figs. 11(c) and 11(e)], the left propagating wavepackets diminish in size and shrink below the low-amplitude cutoff. In addition, these disturbances exhibit pointwise temporal decay.

A significant change in behavior occurs at the larger Reynolds number $Re = 715$ [see Figs. 11(d) and 11(f)]. Wavepackets propagating to the left no longer diminish but instead grow in size, albeit at amplitudes less than those wavepackets propagating to the right. Moreover, solutions exhibit a pointwise temporal growth at fixed streamwise x-locations. For instance, in Fig. 11(f), the disturbance amplitude at $x = -360$ grows every two periods of wall motion. Similarly, at $x = -1250$ and $x = 500$. Thus, subharmonic pointwise temporal growth emerges.

Further evidence of the subharmonic phenomenon and pointwise temporal growth for $\beta > 0.5$ is presented in Fig. 12. The temporal development of the disturbance maximum, $\max_x|\zeta|$, and the size of $|\zeta|$ at the fixed streamwise locations $x = 500$ and $x = -360$, are plotted for those acceleration skewness, β, and Reynolds numbers, Re, modeled in Fig. 11. The evolution of the disturbance maxima, as depicted in Figs. 12(a) and 12(b), further demonstrates the destabilizing effect due to acceleration skewness. At the streamwise location $x = 500$, the temporal evolution of the disturbance is shown to be almost identical in all cases considered [see Figs. 12(c) and 12(d)]. On the time interval shown, disturbances exhibit comparable amplitudes and subharmonic behavior, with pointwise temporal growth observed at $Re = 715$. Moreover, similar behavior emerges at $x = -360$ [see Figs. 12(e) and 12(f)], albeit with a reduction in the disturbance amplitude as the acceleration skewness parameter, β, increases. However, in contrast to the behavior shown for the Stokes layer, notable differences emerge between the pointwise growth rate, μ_0, and the temporal growth rate along the disturbance maximum, μ_m, for the acceleration-skewed flows $\beta = 0.52$ and $\beta = 0.54$. As shown in Fig. 13, the size of μ_m (measured at large time, τ) associated with these two acceleration-skewed flows is significantly greater than the corresponding μ_0, with the latter positive for $Re = 715$. Hence, disturbances associated with flows $\beta = 0.52$ and $\beta = 0.54$ are absolutely unstable for the Reynolds number $Re = 715$, albeit with a pointwise temporal growth rate less than that associated with the disturbance maximum.

Thus, acceleration-skewed flows $\beta \in (0.5, 0.54]$ display both convective and absolute instability. The onset of linear instability

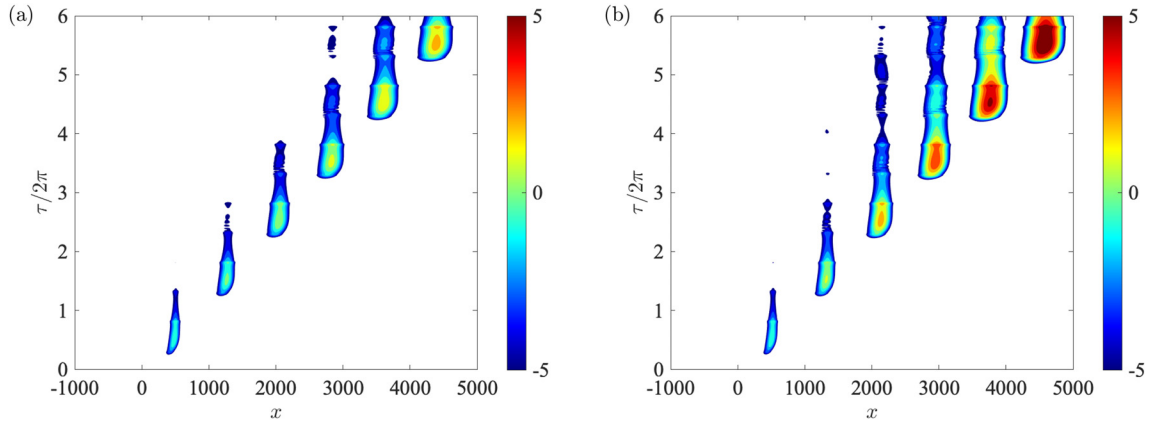

FIG. 8. Spatiotemporal contour plots of the linear disturbance in an acceleration-skewed Stokes layer with $\beta = 0.6$ and $\phi = 1.37$ and Reynolds number (a) $Re = 650$ and (b) $Re = 675$. Contours are based on the logarithm of the absolute valued wall vorticity perturbation, $\ln|\zeta|$, and normalized on $\max_{x,\tau\in[0,2\pi]}|\zeta|$.

coincides with convective instability at a Reynolds number, Re_c, less than that found for the Stokes layer, i.e., $Re_c < Re_{s,c} \approx 708$. Convectively, unstable behavior prevails on a finite interval of Reynolds numbers before absolute instability emerges for $Re \approx Re_{s,c}$. Whether the latter observation holds for acceleration-skewed flows $\beta > 0.54$ is difficult to quantify due to the significant numerical difficulties outlined earlier. However, given the form of the base flow (5b), we predict that absolute instability will occur for a Reynolds number $Re > Re_{s,c} \approx 708 > Re_c$. The acceleration-skewed base flow (5b) can be decomposed as

$$U_B(y,\tau;\beta) = \gamma_1 e^{-y}\sin(\tau+\phi-y) + \sum_{n=2}^{N}\gamma_n e^{-\sqrt{n}y}\sin\left(n(\tau+\phi)-\sqrt{n}y\right), \quad (19)$$

where $\gamma_1 = \alpha < 1$, i.e., the base flow is a linear combination of the scaled Stokes layer (which exhibits absolute instability for $Re = Re_{s,c}$) and higher-order frequency oscillations. Consequently, due to the linearity of the problem, we might anticipate the emergence of absolute instability for all acceleration-skewed flows at sufficiently high Reynolds numbers. Indeed, we might expect absolute instability to develop for Reynolds numbers, Re, near $Re_{s,c}/\alpha$. Given the slow variation in α for acceleration-skewed flows (see Fig. 1), this would explain why absolutely unstable behavior emerges for flows $\beta = 0.52$ and $\beta = 0.54$ at Reynolds numbers $Re \approx Re_{s,c}$.

Figure 14(a) plots the critical Reynolds number, Re_c, for the onset of linear instability and convectively unstable behavior (solid blue line), along with the predicted Reynolds number $Re = Re_{s,c}/\alpha$ for the emergence of absolute instability (dashed red), as a function of the acceleration skewness parameter, β. The dotted horizontal line marks the onset of linear instability in the Stokes layer. [Figure 14(b) depicts equivalent behavior for the velocity-skewed base flow (5c), which is discussed in more detail in Sec. III C.]

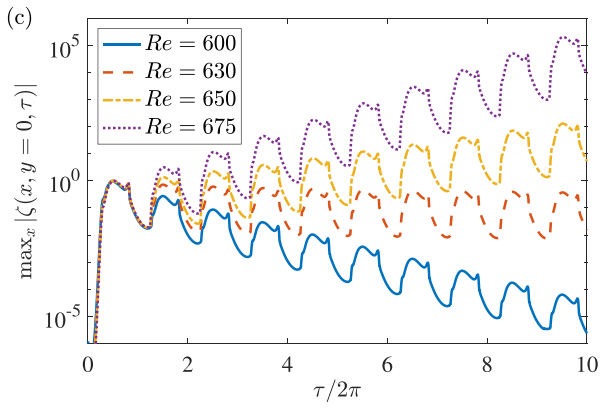

FIG. 9. Temporal development of the maximum amplitude of the wall vorticity perturbation, $\max_x|\zeta|$, with $\beta = 0.6$ and $\phi = 1.37$.

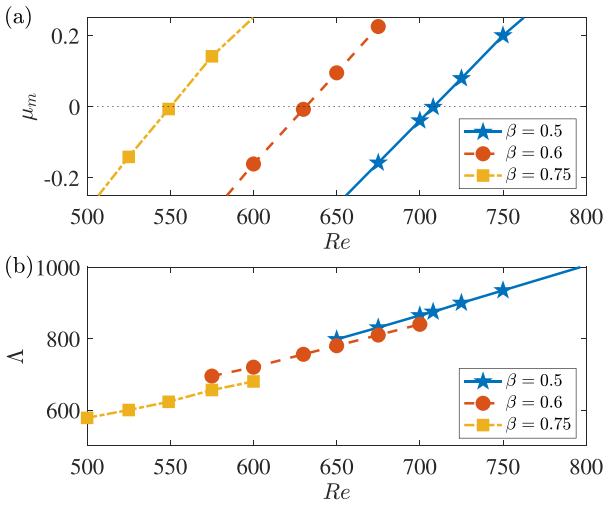

FIG. 10. (a) Large time asymptotic values of the temporal growth rate, μ_m, along the disturbance maximum and (b) streamwise distance, Λ, between neighboring wavepackets as a function of Re. The acceleration skewness parameter $\beta = 0.5$ (solid blue line), $\beta = 0.6$ (dashed red), and $\beta = 0.75$ (chain yellow).

TABLE I. Critical Reynolds numbers, Re_c, for linear instability, with the equivalent Floquet stability calculations given in brackets.[23,24]

	$\beta = \kappa = 0.5$	$\beta = 0.6$	$\beta = 0.75$	$\kappa = 0.6$	$\kappa = 0.75$
Re_c	708.3 (707.8)	631.5 (630.1)	550.2 (548.7)	747.8 (746.1)	881.5 (879.6)

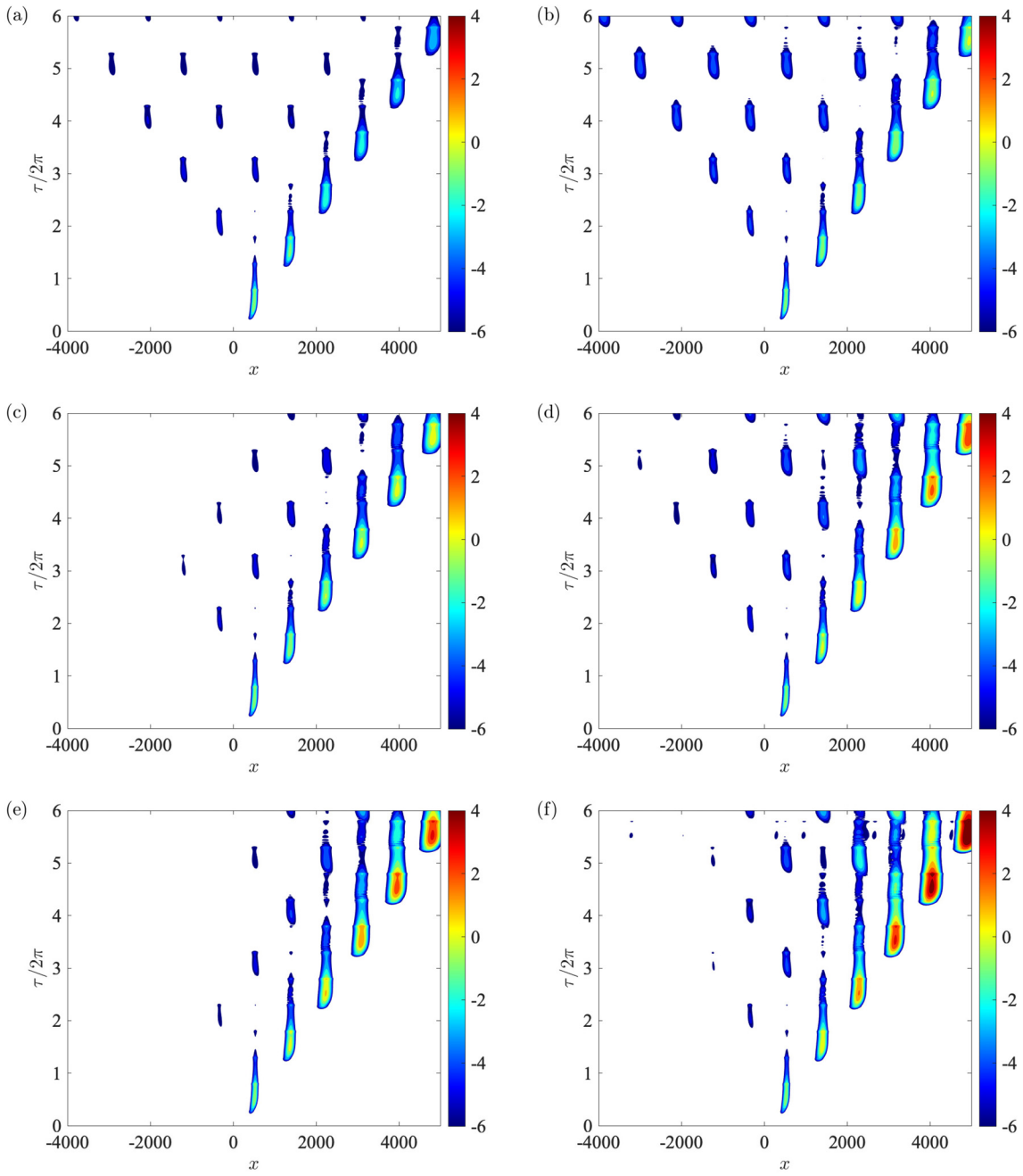

FIG. 11. Spatiotemporal contour plots of linear disturbances in acceleration-skewed Stokes layers $\beta \in [0.5, 0.54]$ with Reynolds number (a), (c), and (e) $Re = 700$ and (b), (d), and (f) $Re = 715$. Contours are based on the logarithm of the absolute valued wall vorticity perturbation, $\ln|\zeta|$, and normalized on $\max_{x,\tau\in[0,2\pi]}|\zeta|$. Disturbances are impulsively excited at $x_f = 0$ and the phase shift, ϕ, is chosen to ensure $U_B(0,0) = 1$. (a) and (b) $(\beta, \phi) = (0.5, \pi/2)$, (c) and (d) $(\beta, \phi) = (0.52, 1.49)$, and (e) and (f) $(\beta, \phi) = (0.54, 1.41)$.

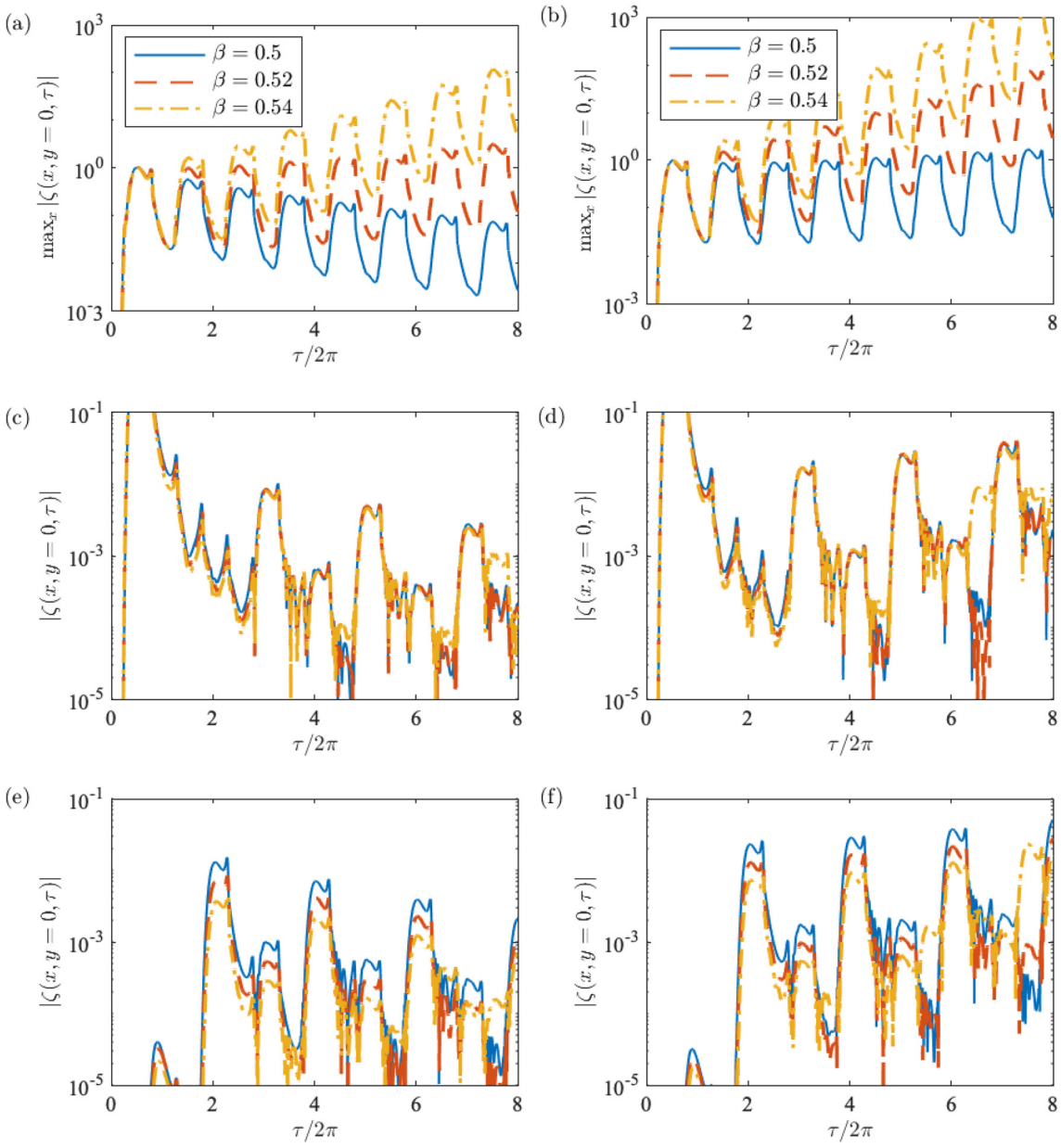

FIG. 12. Temporal development of (a) and (b) the maximum amplitude of the wall vorticity, $\max_x|\zeta|$, (c) and (d) $|\zeta|$ at the fixed streamwise location $x = 500$, and (e) and (f) $|\zeta|$ at $x = -360$. The Reynolds number $Re = 700$ in (a), (c), and (e) and $Re = 715$ in (b), (d), and (f). The acceleration skewness and phase shift $(\beta, \phi) = (0.5, \pi/2)$ (solid blue lines), $(\beta, \phi) = (0.52, 1.49)$ (dashed red), and $(\beta, \phi) = (0.54, 1.41)$ (dotted yellow).

4. Discussion

The above analysis demonstrates the disruptive impact of acceleration skewness on the symmetry of the family tree structure. Pointwise temporal growth is negated, and the onset of linear instability coincides with convective instability, with absolute instability emerging at larger Reynolds numbers. Such observations are expected, given that acceleration skewness establishes asymmetric oscillatory motion and thereby eliminates the antiperiodic nature of the flow. In the absence of acceleration skewness, the Stokes layer is periodic with period 2π and antiperiodic with period π, meaning $U_B(y, \tau + 2\pi) = U_B(y, \tau)$ and $U_B(y, \tau + \pi) = -U_B(y, \tau)$, which implies there is no distinction between the negative (i.e., motion to the left) and positive (i.e., motion to the right) x-directions. Conversely, acceleration-skewed flows are not antiperiodic, with $U_B(y, \tau + \pi) \neq -U_B(y, \tau)$. Thus, the behavior along the negative and positive x-directions is no longer equivalent.

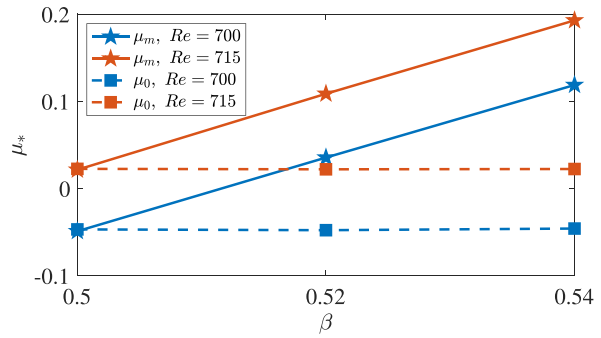

FIG. 13. Large time asymptotic values of the temporal growth rate, μ_m, along the disturbance maximum (solid lines and star markers), and large time asymptotic pointwise growth rate, μ_0, at fixed streamwise locations (dashed lines and square markers), for acceleration-skewed flows $\beta = (0.5, 0.52, 0.54)$ and Reynolds numbers $Re = 700$ (blue) and $Re = 715$ (red).

In acceleration-skewed flows $\beta > 0.5$, disturbance development is predominantly directed to the right and along the positive x-direction. For this family of flows, acceleration skewness induces a flow characterized by short periods of strong accelerating flow with long periods of weak decelerating flow, as illustrated in Fig. 2(c). Moreover, acceleration-skewed flows feature longer and shorter intervals of positive and negative shear stress, respectively [see Fig. 2(e)]. Consequently, regardless of the timing of the impulsive forcing, disturbance development is primarily directed along the positive x-direction for acceleration-skewed Stokes layers $\beta > 0.5$. The reverse is true for $\beta < 0.5$.

C. Velocity-skewed Stokes layer

The analysis of Sec. III B is extended to velocity-skewed flows (5c) specified by the velocity skewness parameter, κ. For $\kappa > 0.5$, this family of oscillatory flows is characterized by short intervals of high, positive velocity and extended intervals of low, negative velocity. Moreover, much like the acceleration-skewed flows $\beta > 0.5$, the velocity-skewed flow experiences longer intervals of positive-valued shear stress (see Fig. 2). The reverse is true for $\kappa < 0.5$. Figure 15 displays the spatiotemporal development of two disturbances impulsively excited at $x_f = 0$ for $\kappa = 0.6$ and the unstable Reynolds number $Re = 746$. (Recall that velocity skewness is stabilizing and raises the critical Reynolds number, Re_c, for linear instability.[24]) The phase shift, ϕ, in Eq. (5c), is again chosen to ensure $U_B(0,0) = 1$ in Fig. 15(a) and $U_B(0,0) = -1$ in Fig. 15(b). Much like those acceleration-skewed flows modeled above, disturbance development is directed to the right, corresponding to the direction that the velocity attains a peak value. Although each disturbance displays unstable behavior, with the disturbance maximum passing through the right-most wavepackets in Fig. 15(a) and second to right in Fig. 15(b), each disturbance exhibits pointwise temporal decay at fixed streamwise x-locations. Consequently, similar to the acceleration-skewed flows, the onset of linear instability coincides with convective instability.

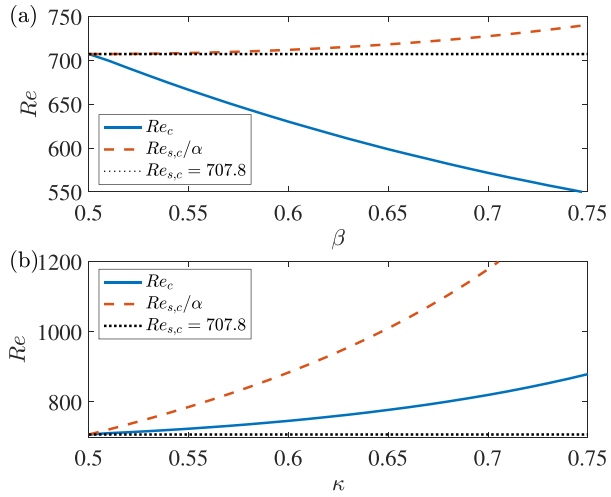

FIG. 14. Critical Reynolds numbers, Re_c, for linear instability[23,24] (solid blue lines), predicted Reynolds number $Re = Re_{s,c}/\alpha$ for the onset of absolute instability (dashed red), and $Re_{s,c} = 708$ for the Stokes layer (dotted black). (a) Acceleration-skewed flows, β, and (b) velocity-skewed flows, κ.

Additional disturbances (not shown here) were simulated at higher Reynolds numbers ($750 \le Re \le 800$) for $\kappa = 0.6$. However, in each case, convectively unstable behavior prevailed. Like the study into acceleration-skewed flows, establishing disturbance development at higher Reynolds numbers was difficult due to the considerable temporal growth observed along the disturbance maximum. Nevertheless, recognizing that velocity-skewed flows (5c) can be decomposed into a form comprising a scaled Stokes layer with higher-order frequency oscillations akin to Eq. (19), we predict that absolute instability is likely to emerge for a Reynolds number Re near $Re_{s,c}/\alpha$, where $Re_{s,c}/\alpha > Re_c > Re_{s,c} \approx 708$. (See the solid blue and dashed red lines in Fig. 14(b) for Re_c and $Re_{s,c}/\alpha$, respectively.) Given the rapid variation in α for velocity-skewed flows (see Fig. 1), we might expect absolute instability to appear for $Re = Re_{s,c}/\alpha \approx 885$ for $\kappa = 0.6$. A significantly higher Reynolds number than what we could accurately simulate for this velocity-skewed flow.

For the weaker velocity-skewed flow $\kappa = 0.52$, disturbances were established for Reynolds numbers $Re = (700, 725, 750)$ to test the viability of our approach in predicting the onset of absolute instability. Figure 16 plots the large time asymptotic temporal growth rate, μ_m, of the disturbance maximum (star markers), along with the large time asymptotic pointwise growth rate, μ_0, at fixed x-locations (square markers). A line of best fit connects each set of markers. The two vertical chain lines indicate the critical Reynolds number, Re_c, for linearly unstable behavior (as computed via Floquet theory[24]) and the predicted Reynolds number, $Re_{s,c}/\alpha$, for absolute instability. The pointwise growth rate, μ_0, increases linearly with the Reynolds number, Re, with a positive-valued μ_0 realized for $Re \approx Re_{s,c}/\alpha$. Thus, $Re \approx Re_{s,c}/\alpha$ gives a reasonable estimate for absolute instability, at least for weak velocity-skewed flows.

Figure 17 displays the variation in the large time asymptotic temporal growth rate, μ_m, and the corresponding streamwise distance, Λ, between neighboring wavepackets in the spatiotemporal plane, as a function of the Reynolds number, Re. Solutions are matched to the velocity-skewed flows $\kappa = 0.5$ (i.e., Stokes layer), $\kappa = 0.6$, and $\kappa = 0.75$. Results demonstrate the significant stabilizing effect due to velocity skewness, with the critical Reynolds numbers, Re_c, agreeing with Floquet stability calculations[24] (see Table I). In addition, similar

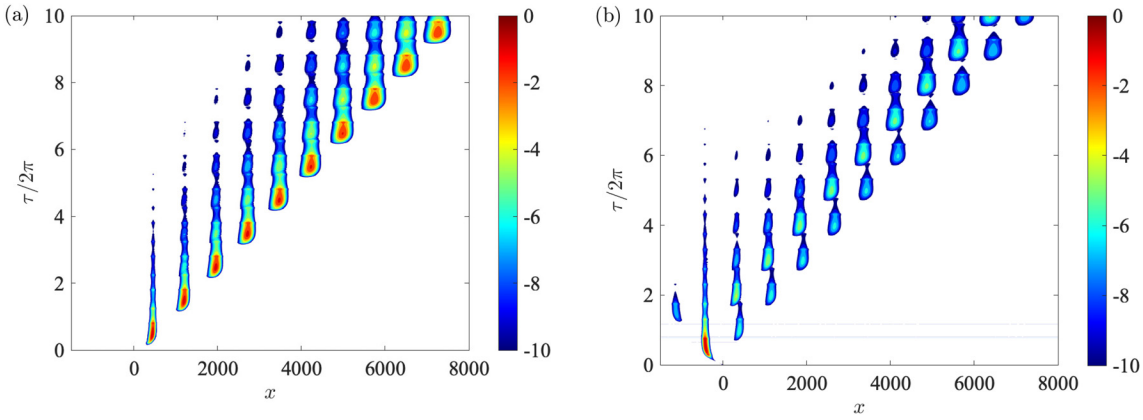

FIG. 15. Spatiotemporal contour plots of the linear disturbance in a velocity-skewed Stokes layer with $\kappa = 0.6$ and Reynolds number $Re = 746$ and phase shift (a) $\phi = 0$ and (b) $\phi = \pi/2$. Contours are based on the logarithm of the absolute valued wall vorticity perturbation, $\ln|\zeta|$, and normalized on $\max_{x,\tau\in[0,2\pi]}|\zeta|$.

to the acceleration-skewed flow, the distance Λ increases linearly with Re and decreases with κ. However, the reduction in Λ is far more pronounced for these velocity-skewed flows compared with those acceleration-skewed flows plotted in Fig. 10.

IV. CONCLUSIONS

A numerical study has been undertaken on the evolution of two-dimensional, linear disturbances impulsively excited in acceleration-skewed and velocity-skewed Stokes layers. This extends earlier investigations based on Floquet theory,[23,24] with the aim to determine whether linearly unstable behavior corresponds to convective or absolute instability. It is well-established that linear disturbances in the symmetric Stokes layer are characterized by a family tree wavepacket structure and subharmonic phenomena, with the onset of linear instability coinciding with absolute instability.[1,10]

Following the methodology of Ramage *et al.*,[1] we numerically simulated disturbance development and analyzed the effects of skewness. Both acceleration and velocity skewness were found to disrupt the family tree wavepacket formation, with disturbances primarily convecting in the direction of the highest acceleration or highest velocity. For acceleration-skewed flows characterized by the skewness parameter β, linear disturbances in flows $\beta > 0.5$ were directed to the right, regardless of the phase that disturbances were initially excited. The same was true for velocity-skewed flows $\kappa > 0.5$, with disturbances propagating to the left for flows matched to $\beta < 0.5$ or $\kappa < 0.5$.

At the onset of linear instability, the pointwise, subharmonic temporal growth observed for the Stokes layer[1] was replaced by pointwise temporal decay. In contrast to the symmetric Stokes layer, where critical linear instability coincides with absolute instability, disturbances in acceleration-skewed and velocity-skewed oscillating flows exhibited convectively unstable behavior. Nonetheless, results suggest that convective instability is only prevalent on a finite interval of Reynolds numbers, and absolute instability eventually emerges at sufficiently large Reynolds numbers. However, the pointwise temporal growth is significantly less than that associated with the disturbance maximum.

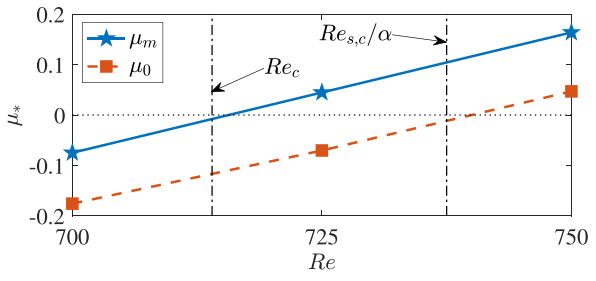

FIG. 16. Large time asymptotic temporal growth rate, μ_m, along the disturbance maximum (solid line and star markers), and large time asymptotic pointwise growth rate, μ_0, at fixed streamwise locations (dashed line and square markers), for the velocity-skewed flow $\kappa = 0.52$ and Reynolds numbers $Re = 700$, $Re = 725$, and $Re = 750$. The vertical chain lines indicate the critical Reynolds number, Re_c, for the onset of linear instability[24] and the predicted Reynolds number, $Re_{s,c}/\alpha$, for absolute instability.

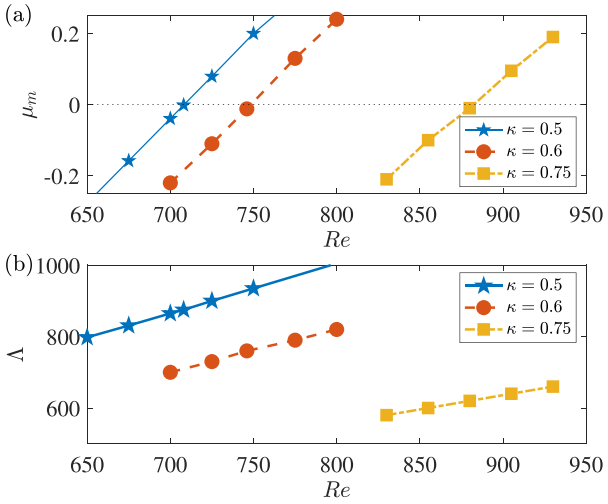

FIG. 17. (a) Large time asymptotic temporal growth rate, μ_m, along the disturbance maximum, and (b) streamwise distance, Λ, between neighboring wavepackets as a function of Re. The velocity skewness parameter $\kappa = 0.5$ (solid blue line), $\kappa = 0.6$ (dashed red), and $\kappa = 0.75$ (chain yellow).

The above study focused on two-dimensional linear disturbances, neglecting three-dimensional and nonlinear effects. In addition to growing or decaying over one period of oscillation (as determined by the Floquet exponent, μ), linear disturbances can experience intervals of substantial growth during the wall motion, leading to large variations in magnitude. Consequently, maintaining disturbances at a level small enough to prevent nonlinearity poses a significant challenge. Indeed, experimental investigations on the symmetric Stokes layer show that transition to turbulence occurs at Reynolds numbers considerably lower than those associated with the onset of linear instability.[15–18]

Vittori and co-workers[12–14] demonstrated that transition to turbulence can be initiated by a resonance mechanism, where wall imperfections amplify disturbance growth during certain phases of the wall motion. They identified four flow regimes, with each occurring before the onset of the Floquet linear instability: a laminar regime and a disturbed laminar regime where the flow is locally unstable during parts of the oscillatory cycle, followed by an intermittently turbulent regime and a fully developed turbulent regime. Using a momentary stability criterion (or quasi-steady flow approximation),[45] Blondeaux and Vittori[46] determined the Reynolds number range in which the Stokes layer experiences these four regimes.

Thomas *et al.*[32] proposed an alternative strategy to model the oscillatory flow by superimposing the Stokes layer with a low-amplitude, high-frequency harmonic. This approach aimed to replicate experimental imperfections that introduce low-level noise into an otherwise purely sinusoidal oscillatory motion. A Floquet analysis based on this modulated oscillatory flow revealed that the critical Reynolds number for linear instability was reduced by half, aligning the theoretical predictions with experimental observations.

Future investigations of skewed oscillatory flows could build upon the results of this study and the aforementioned earlier works by exploring three-dimensional and nonlinear effects and high-frequency modulation.

ACKNOWLEDGMENTS

The authors did not receive support from any organization for the submitted work.

AUTHOR DECLARATIONS

Conflict of Interest

The authors have no conflicts to disclose.

Author Contributions

Christian Thomas: Conceptualization (lead); Investigation (lead); Methodology (equal); Writing – original draft (lead); Writing – review & editing (equal). **Alexander Pretty:** Conceptualization (supporting); Investigation (supporting); Methodology (equal); Writing – original draft (supporting); Writing – review & editing (equal).

DATA AVAILABILITY

The data that support the findings of this study are available from the corresponding author upon reasonable request.

REFERENCES

[1]A. Ramage, C. Davies, C. Thomas, and M. Togneri, "Numerical simulation of the spatiotemporal development of linear disturbances in Stokes layers: Absolute instability and the effects of high-frequency harmonics," Phys. Rev. Fluids **5**, 103901 (2020).
[2]S. H. Davis, "The stability of time-periodic flows," Annu. Rev. Fluid Mech. **8**, 57–74 (1976).
[3]S. Cowley, "High frequency Rayleigh instability analysis of Stokes layers," in *Stability of Time-Dependent and Spatially Varying Flows*, edited by D. L. Dwoyer and M. Y. Hussaini (Springer, 1987), pp. 261–275..
[4]P. Hall, "On the stability of the Stokes layers at high Reynolds numbers," J. Fluid Mech. **482**, 1–15 (2003).
[5]J. Luo and X. Wu, "On the linear instability of a finite Stokes layer: Instantaneous versus Floquet modes," Phys. Fluids **22**, 054106 (2010).
[6]C. Von Kerczek and S. H. Davis, "Linear stability theory of oscillatory Stokes layers," J. Fluid Mech. **62**, 753–773 (1974).
[7]P. Hall, "The linear stability of flat Stokes layers," Proc. R. Soc. Lond. A **359**, 151–166 (1978).
[8]P. J. Blennerhassett and A. P. Bassom, "The linear stability of flat Stokes layers," J. Fluid Mech. **464**, 393–410 (2002).
[9]A. Pretty, C. Davies, and C. Thomas, "Onset of absolutely unstable behaviour in the Stokes layer: A Floquet approach to the Briggs method," J. Fluid Mech. **928**, A23 (2021).
[10]C. Thomas, C. Davies, A. P. Bassom, and P. J. Blennerhassett, "Evolution of disturbance wavepackets in an oscillatory Stokes layer," J. Fluid Mech. **752**, 543–571 (2014).
[11]A. Ramage, "Linear disturbance evolution in the semi-infinite Stokes layer and related flows," Ph.D. thesis (School of Mathematics, Cardiff University, 2017).
[12]P. Blondeaux and G. Vittori, "Wall imperfections as a triggering mechanism for Stokes-layer transition," J. Fluid Mech. **264**, 107–135 (1994).
[13]R. Verzicco and G. Vittori, "Direct simulation of transition in Stokes boundary layers," Phys. Fluids **8**, 1341–1343 (1996).
[14]G. Vittori and R. Verzicco, "Direct simulation of transition in an oscillatory boundary layer," J. Fluid Mech. **371**, 207–232 (1998).
[15]M. Hino, M. Sawamoto, and S. Takasu, "Experiments on transition to turbulence in an oscillatory pipe flow," J. Fluid Mech. **75**, 193–207 (1976).
[16]M. Clamen and P. Minton, "An experimental investigation of flow in an oscillating pipe," J. Fluid Mech. **81**, 421–431 (1977).
[17]R. Akhaven, R. D. Kamm, and A. H. Shapiro, "An investigation of transition to turbulence in bounded oscillatory flows. Part 1. Experiments," J. Fluid Mech. **225**, 395–422 (1991).
[18]D. M. Eckmann and J. B. Grotberg, "Experiments on transition to turbulence in oscillatory pipe flow," J. Fluid Mech. **222**, 329–350 (1991).
[19]B. Pier and P. Schmid, "Linear and nonlinear dynamics of pulsatile channel flow," J. Fluid Mech. **815**, 435–480 (2017).
[20]D. Biau, "Transient growth of perturbations in Stokes oscillatory flows," J. Fluid Mech. **794**, R4 (2016).
[21]B. Pier and P. Schmid, "Optimal energy growth in pulsatile channel and pipe flows," J. Fluid Mech. **926**, A11 (2021).
[22]D. Xu, B. Song, and M. Avila, "Non-modal transient growth of disturbances in pulsatile and oscillatory pipe flows," J. Fluid Mech. **907**, R5 (2021).
[23]C. Thomas, "The linear stability of an acceleration-skewed oscillatory Stokes layer," J. Fluid Mech. **895**, A27 (2020).
[24]C. Thomas, "Effects of velocity skewness on the linear stability of the oscillatory Stokes layer," Phys. Fluids **33**, 034104 (2021).
[25]C. Thomas, A. P. Bassom, P. J. Blennerhassett, and C. Davies, "Direct numerical simulations of small disturbances in the classical Stokes layer," J. Eng. Math. **68**, 327–338 (2010).
[26]P. J. Blennerhassett and A. P. Bassom, "The linear stability of high-frequency oscillatory flow in a channel," J. Fluid Mech. **556**, 1–25 (2006).
[27]P. J. Blennerhassett and A. P. Bassom, "The linear stability of high-frequency flow in a torsionally oscillating cylinder," J. Fluid Mech. **576**, 491–505 (2007).
[28]C. Thomas, A. P. Bassom, P. J. Blennerhassett, and C. Davies, "The linear stability of oscillatory Poiseuille flow in channels and pipes," Proc. R Soc. A **467**, 2643–2662 (2011).
[29]C. Thomas, A. P. Bassom, and P. J. Blennerhassett, "The linear stability of oscillating pipe flow," Phys. Fluids **24**, 014106 (2012).
[30]P. Huerre and P. Monkewitz, "Local and global instabilities in spatially developing flows," Annu. Rev. Fluid Mech. **22**, 473–537 (1990).

[31]C. Davies and P. Carpenter, "A novel velocity-vorticity formulation of the Navier–Stokes equations with applications to boundary layer disturbance evolution," J. Comput. Phys. **172**, 119–165 (2001).
[32]C. Thomas, P. J. Blennerhassett, A. P. Bassom, and C. Davies, "The linear stability of a Stokes layer subjected to high frequency perturbations," J. Fluid Mech. **764**, 193–218 (2015).
[33]R. J. Briggs, *Electron-Stream Interaction with Plasmas* (The MIT Press, 1964).
[34]L. Brevdo and T. J. Bridges, "Absolute and convective instabilities of temporally oscillating flows," Z angew. Math. Phys. **48**, 290–309 (1997).
[35]O. Madsen, "Stability of a sand bed under breaking waves," in *Proceedings of the Fourteenth Conference on Coastal Engineering* (ASCE, 1974), pp. 776–794.
[36]J. S. Ribberink and A. A. Al-Salem, "Sheet flow and suspension of sand in oscillatory boundary layers," Coast. Eng. **25**, 205–225 (1995).
[37]M. Dibajnia and A. Watanabe, "Transport rate under irregular sheet flow conditions," Coast. Eng. **35**, 167–183 (1998).
[38]T. Drake and J. Calantoni, "Discrete particle model for sheet flow sediment transport in the nearshore," J. Geophys. Res. **106**(C9), 19859–19868, https://doi.org/10.1029/2000JC000611 (2001).
[39]P. Nielsen and D. Callaghan, "Shear stress and sediment transport calculations for sheet flow under waves," Coast. Eng. **47**, 347–354 (2003).
[40]A. Watanabe and S. Sato, "A sheet-flow transport rate formula for asymmetric forward-leaning waves and currents," in *Proceedings of 19th Conference on Coastal Engineering* (ASCE, 2004) pp. 1703–1714.
[41]T. O'Donoghue and S. Wright, "Concentrations in oscillatory sheet flow for well sorted and graded sands," Coast. Eng. **50**, 117–138 (2004).
[42]T. Abreu, P. A. Silva, F. Sancho, and A. Temperville, "Analytical approximate wave form for asymmetric waves," Coast. Eng. **57**, 656–667 (2010).
[43]P. Scandura, C. Faraci, and E. Foti, "A numerical investigation of acceleration-skewed oscillatory flows," J. Fluid Mech. **808**, 576–613 (2016).
[44]D. A. van der A, T. O'Donoghue, A. G. Davies, and J. S. Ribberink, "Experimental study of the turbulent boundary layer in acceleration-skewed oscillatory flow," J. Fluid Mech. **684**, 251–283 (2011).
[45]P. Blondeaux and G. Seminara, "Transizione incipiente al fondo di un'onda di gravita," Atti Accad. Naz. Lincei **67**(6), 408–417 (1979); available at https://eudml.org/doc/288696.
[46]P. Blondeaux and G. Vittori, "Revisiting the momentary stability analysis of the Stokes boundary layer," J. Fluid Mech. **919**, A36 (2021).